Parcellation of the primate prefrontal cortex by cognitive control operations

Xuanyu Wang[1,2], Daniel Hähnke[1], Andreas Nieder[3], Simon N. Jacob[1]*

[1]Translational NeuroTechnology Laboratory, Department of Neurosurgery, Klinikum rechts der Isar, Technical University of Munich

[2]Graduate School of Systemic Neurosciences, Ludwig-Maximilians-University Munich

[3]Animal Physiology, Institute of Neurobiology, University of Tübingen

* Correspondence: simon.jacob@tum.de

Abstract

Modular organization, the division of the cerebral cortex into functionally distinct subregions, is well established in the primate sensorimotor cortex, but debated in the cognitive association cortex, including the lateral prefrontal cortex (PFC). So far, single-unit recordings have not confirmed the prefrontal rostro-caudal gradients observed in neuroimaging and neuroanatomical experiments. To bridge these microscale and macroscale perspectives, we obtained microelectrode recordings with twice the spatial coverage of conventional studies from the PFC of monkeys engaged in a working memory task. Neighboring electrodes shared task-related neural dynamics that were stable across recording sessions and formed spatially continuous, mesoscale clusters with distinct local and long-range fronto-parietal connectivity. Spiking activity was cluster-specific and related to either the encoding, maintenance or decoding of working memory content. Our findings support parcellation of the PFC by cognitive control operations rather than by processed information, indicating that modularity is a fundamental architectural principle across the primate cortex.

Introduction

Whether brain function is mirrored in brain structure is one of the oldest and most fundamental questions in neuroscience (Brodmann, 1909; Kanwisher, 2010; Lashley, 1950). Could the mind's functional modules, or the "modularity of the mind," be reflected in the brain's anatomical and physiological architecture, or the "modularity of the brain"? Answering this question would provide deep insights into the relationship between mental processes and their neuronal underpinnings.

An ordered spatial organization that links brain structure to brain function is characteristic of the sensory and the motor regions and has been amply described in the visual system (retinotopy) (Hubel & Wiesel, 1977; Steel et al., 2024; Talbot & Marshall, 1941), the auditory system (tonotopy) (Bandyopadhyay et al., 2010; Humphries et al., 2010; Schreiner et al., 2000), the somatosensory system (somatotopy, sensory homunculus) (Penfield & Boldrey, 1937) and in the motor system (motor homunculus) (Gordon et al., 2023; Penfield & Boldrey, 1937). These topographical maps are the result of spatially ordered afferent connections from the sensors and efferent projections to the effectors. Thus, the sensory and motor cortices are organized as spatial replica of the continuous physical space they have evolved to internalize (Kaas, 1997).

Cognitive theories also propose an innate modular structure for the mind (Fodor, 1983). In this architecture, distinct subdivisions, each responsible for a different mental function, operate largely independently of each other and process specific types of information. Examples of such derived functional modules are found in the ventral visual pathway for perceiving faces (fusiform face area, (Kanwisher et al., 1997)), places (parahippocampal place area, (Epstein & Kanwisher, 1998)) and written words (visual word form area, (Mccandliss et al., 2003)), in the posterior parietal cortex for processing number (Harvey et al., 2013) and in the frontotemporal cortex for understanding language (Fedorenko et al., 2011).

However, whether these organizational principles apply to the lateral prefrontal cortex (PFC) and other associative cortical areas that border the domain-specific modules (Fedorenko et al., 2013) and are crucial for domain-general, higher-order cognitive functions remains controversial. The neuronal representations of task-related variables in associative cortical areas are typically high-dimensional, extending beyond the two- or three-dimensional geometry of physical space (Tye et al., 2024). In contrast to sensory or motor cortical neurons that are tuned to specific stimulus or movement features (pure selectivity), PFC neurons are recurrently connected into spatially overlapping (Xie et al., 2022), flexibly forming and disbanding ensembles (Hanganu-Opatz et al., 2023) that share similar tuning properties and respond to multiple cognitive variables (mixed selectivity) (Aoi et al., 2020; Rigotti et al., 2013; Tye et al., 2024). Models of prefrontal computation therefore explicitly or implicitly adopt the hypothesis that PFC neurons form a homogenous, interconnected network, where the physical location of individual neurons is not informative about their function and, consequently, there is no innate modularity (**Fig. 1a**) (Miller et al., 2018; Mongillo et al., 2008; Stokes, 2015).

Contrary to this microscale view, a large body of evidence indicates that the PFC is modularly structured on the macroscale, i.e., in the millimeter to centimeter range. Tracing and structural imaging studies have identified subdivisions in lateral PFC with distinct anatomical connectivity patterns (Jung et al., 2022; Petrides & Pandya, 1999; Rapan et al., 2023). Functional and lesion studies point to a rostro-caudal hierarchical organization of the lateral PFC with actions represented in descending order of abstraction, i.e., from abstract action control (frontal polar cortex) (Mansouri et al., 2017) to concrete motor responses (dorsal premotor cortex) (Koechlin et al., 2003). Changes in task-engagement and in the capacity for learning-related plasticity develop along a similar trajectory (Badre & D'Esposito, 2007, 2009; Riley et al., 2018).

So far, no equivalent of this macro-architecture has been described at the single-neuron and local microcircuit level, likely because conventional microelectrode recordings cover a few millimeters at most and therefore do not sample from a large enough cortical area (Lundqvist et al., 2023; Wang et al., 2023). Here, we bridged across the disconnected microscale and macroscale perspectives and analyzed extracellular measurements from the primate PFC that spanned an area twice that of conventional multi-electrode arrays. Using working memory as a paradigmatic example of prefrontal higher cognition, we report evidence for a modular organization of the lateral PFC with parcellation not by the content of the processed information (**Fig. 1b**), but instead by the type of cognitive operation performed on this information (**Fig. 1c**).

Results

Working memory related oscillatory burst activity

We obtained extracellular multi-electrode recordings from the (right-hemispheric) frontoparietal association cortex of two monkeys performing a delayed-match-to-numerosity task, which required the animals to memorize the number of dots (i.e., numerosity) in a visually presented sample and resist an interfering distracting numerosity (Jacob & Nieder, 2014; Lin et al., 2023) (**Fig. 2a**). In each recording session, four pairs of single-contact microelectrodes were acutely inserted through grids with 1 mm inter-electrode spacing into the lateral PFC and the ventral intraparietal area (VIP) (**Fig. 2b**). The diameter of the grids (14 mm) allowed us to sample from cortical areas that extended beyond the areas covered by typical planar microelectrode arrays (Chapeton et al., 2022; Eisenkolb et al., 2023; Lundqvist et al., 2023) and still retain single-neuron resolution at each electrode. We analyzed a total of 616 PFC electrodes (368 and 248 in monkey R and W, respectively) and 614 VIP electrodes (376 and 238 in monkey R and W, respectively) across 78 sessions (47 and 31 from monkey R and W, respectively).

We first characterized neuronal activity patterns at individual electrodes using the local field potential (LFP, extracellular voltage signal low-pass filtered at 170 Hz). LFPs capture the volume summation of oscillatory, synchronized population activity in the local neuronal circuit (Buzsáki et al., 2012). Their lateral span of several hundred micrometers (Lindén et al., 2011), comparative stability across sessions and comprehensive account of ongoing network activity make LFPs well-suited to explore the spatial and functional organization of the recorded area at the mesoscale (Chapeton et al., 2022; Katzner et al., 2009; Wang, 2010).

Raw LFP traces were segmented by trials, spectrally transformed (Moca et al., 2021) and normalized to the average band power of 9 previous trials and the current trial. At the single-trial level, prefrontal oscillatory activity was not sustained throughout the trial, but instead composed of sparse, short-lived peaks in narrow-band LFP power (bursts) (**Fig. 2c**) (Lundqvist et al., 2016; Miller et al., 2018). We defined LFP bursts as increases in instantaneous power that exceeded the mean by two standard deviations. We focused on two frequency bands, gamma (60 – 90 Hz) and beta (15 – 35 Hz), because of their well-documented association with the encoding, maintenance and decoding of working memories in primate prefrontal and parietal cortex (Jacob et al., 2018; Lundqvist et al., 2018; Lundqvist et al., 2016). 2D Gaussian kernels were fitted to the local maxima to quantify the bursts' spectrotemporal properties. Both gamma and beta bursts lasted for approximately two cycles (mean and standard deviation: gamma: 2.5 ± 1.1 cycles / 33.9 ± 14.3 ms, beta: 1.9 ± 0.8 cycles / 76.4 ± 38.3 ms; **Fig. 2d**). The distribution of inter-burst intervals showed modes at zero and one cycle, indicating temporal overlap but spectral separation of oscillatory bursting activity (**Fig. 2e**). LFP bursts were tightly and systematically coupled across frequency bands (Canolty & Knight, 2010), with gamma bursts preferentially occurring at the troughs of beta oscillations and beta bursts preferring the troughs in the alpha (8 – 16 Hz) and peaks in

the delta frequency band (2 – 4 Hz) (**Fig. 2f**). In both regions, this phase-coupling was fixed and independent of trial time (**Fig. S1a**) and sample information (numerosity) (**Fig. S1b**).

Next, we quantified the temporal evolution of bursts by averaging step functions that captured the temporal duration of each burst across trials. Different trial events were clearly reflected in the burst probability time courses in both areas (**Fig. 2g**). The probability of beta bursts in particular increased sharply following the onset and offset of visual stimuli (sample and distractor numerosities). Notably, while the latency of sample-triggered beta bursts was the same in PFC and VIP (mean and standard error of mean: 117 ± 29 ms and 116 ±41 ms, respectively; $p = 0.87$, paired t-Test), distractor-triggered bursts occurred significantly later in PFC than in VIP (149 ± 21 ms and 133 ± 28 ms, respectively; $p < 0.001$, paired t-Test), in line with distinct involvement of these regions during memory interference (Jacob & Nieder, 2014). In addition to these event-locked transients, the probability of beta bursts declined during the presentation of the sample and distractor and increased during the memory delays. Gamma bursts, in contrast, were more frequent during presentation of the sample and distractor and decreased during the memory delays. A similar alternation in gamma-beta bursting during working memory was reported previously (Lundqvist et al., 2023; Lundqvist et al., 2018; Lundqvist et al., 2016). In trials without the distractor, the event-locked responses were absent, while the remaining time course was remarkably similar to trials with distractors (**Fig. 2h**).

Finally, to investigate how bursts in oscillatory activity related to spiking activity, we extracted multi-unit activity (MUA; high-pass filtered extracellular voltage signal), at each electrode (271 and 158 PFC multi-units from monkey R and W, respectively; 209 and 112 VIP multi-units from monkey R and W, respectively). Gamma, but not beta, bursts were accompanied by significantly elevated spiking rates in both regions ($p < 0.001$, paired t-Test; **Fig. 2i**). Prefrontal spiking occurring inside gamma and beta bursts was more strongly phase-coupled, i.e., synchronized, to local oscillatory activity across all frequencies than spiking occurring outside of bursts (**Fig. 2j**). For these analyses, we chose the measure of pairwise phase consistency (PPC) (Vinck et al., 2010) because it is free of biases caused by unbalanced numbers of spikes inside and outside of bursts. As expected, spike-field locking was distance-dependent, i.e., it decayed with increasing distance between electrode pairs (**Fig. 2j**). Remarkably, the difference in synchrony between spiking inside and outside of bursts was preserved across regions (locking of PFC spikes inside/outside of bursts to VIP oscillations; **Fig. 2k**), ruling out passive volume-spreading of oscillatory activity across electrodes and “bleeding” of spiking signals into lower frequency bands as explanatory factors. Multi-unit spiking and LFP burst activity both tracked sample numerosity. However, whereas spiking activity showed peaked tuning functions with tuning preferentially to numerosities 1 and 4 (border effect) in the sense of labeled line coding (Jacob & Nieder, 2014; Jacob et al., 2016; Nieder et al., 2002), burst probability increased with number in the majority of prefrontal and parietal electrodes (**Fig. 2l**).

Together, these findings suggest that bursts of oscillatory activity in frontoparietal cortex represent transient, probabilistic and task-modulated “on states” with elevated and synchronized spiking in local and long-range neuronal circuits.

Spatiotemporal patterns of prefrontal oscillatory activity

Next, we asked whether LFP burst patterns varied systematically across the prefrontal recording field. Across recording sessions, the spatial layout of recording sites changed repeatedly, allowing us to reconstruct a flattened, subject-specific map of the experimentally sampled PFC with significantly broader spatial coverage (monkey R: 6×10 mm^2, **Fig. 3a, b**; monkey W: 9×10 mm^2, **Fig. S3a, b**) than can be achieved using smaller planar multielectrode arrays implanted in human or non-human primate cortex (Chapeton et al., 2022; Eisenkolb et al., 2023; Lundqvist et al., 2023). All subsequent analyses were performed for each monkey individually to account for interindividual differences in cortical anatomy and electrode positioning. In each analysis step, we report results from monkey R first, followed by monkey W.

Burst patterns were calculated for each recording site separately by pooling all recordings performed at a given site and averaging burst probabilities across conditions (n = 4 sample and n = 4 distractor numerosities) and sessions. Burst patterns in monkey R were highly specific for individual recording sites (n = 31) with clear differences between electrodes in bursting activity within and across bands (**Fig. 3c**). Importantly, however, burst patterns of adjacent electrodes were very similar (**Fig. 3d**). Sample numerosity presentation triggered a peak of gamma bursting in the ventral PFC, whereas beta bursts mainly appeared in more dorsal electrodes. Both clusters were already apparent in the fixation epoch (pre-sample), suggesting pre-existing task-independent determinants (pre-structure). In the first memory delay, gamma bursting activity moved to a posterior cluster. During distractor numerosity presentation, gamma and beta bursting reappeared again in the same clusters as during the sample. Beta bursts were generally sparse during the memory delays, with a notable exception in the most posterior electrodes in the second memory preceding the test (**Fig. 3d**).

To quantify burst pattern similarity between electrodes, we calculated covariance matrices of gamma and beta burst probability across all recording sites and performed hierarchical agglomerative clustering on the covariance summed across the two frequency bands (**Fig. 3e**). Maximally separated n clusters were then drawn from the resulting dendrogram. The optimal number of clusters was determined using split-half reliability (**Fig. S2**): covariance matrices were calculated using 100 random split-halves (trial subsampling at each PFC recording site) and hierarchically clustered. Clustering reliability was defined as the percentage of recording sites consistently assigned to the same cluster and calculated as a function of the number of selected clusters (**Fig. S2a**). To determine statistical significance, we generated a null distribution for the clustering reliability by shuffling across locations 10 times for each split-half, leading to 1000 samples. We then compared the observed clustering reliability to the 95 % confidence interval (CI)

of this null distribution. Clustering by beta bursts was more consistent than clustering by gamma bursts. The most reliable clustering was obtained with both frequency bands combined (**Fig. S2b**). Reliability dropped markedly when choosing more than three clusters, which we therefore determined to be the optimal number. Parcellation of the prefrontal recording field in monkey R in this way revealed a ventral cluster (#1, 98 electrodes across 9 sites), corresponding to the sites with strong gamma bursting during sample and distractor presentation; a dorsal cluster (#2, 199 electrodes across 18 sites), corresponding to the sites with strong beta bursting during sample and distractor presentation; and a posterior cluster (#3, 71 electrodes across 4 sites), corresponding to the sites with prominent gamma and beta bursting during the memory delays (**Fig. 3f**). Although no spatial information was used for clustering, the resulting clusters were remarkably continuous with no isolated, interspersed electrodes, supporting a close link between oscillatory neuronal activity (bursts) and prefrontal cortical network structure.

The prefrontal recording sites in monkey W were more posterior (**Fig. S3a, b**), but also showed frequency-band, trial-epoch and electrode-specific LFP bursting patterns (**Fig. S3c**) that allowed clustering (**Fig. S3d, e**). In contrast to monkey R, however, clustering reliability decreased smoothly (**Fig. S3f, g**), pointing to a more gradient-like, rather than sharply demarcated, modular spatial organization in the recorded area.

Local and long-range connectivity of prefrontal clusters

We now investigated whether the cluster-specific LFP activity would also be mirrored in cluster-specific local and long-range connectivity (Chapeton et al., 2022) (**Fig. 4**). First, we computed bivariate LFP-LFP Granger Causality (GC) between simultaneously recorded PFC electrode pairs (Granger, 1969). To control for effects of differing physical distance and spatial decay of oscillatory signals between electrodes (Buzsáki et al., 2012; Wang, 2010), we only included electrode pairs separated by 3 or 4 mm. This allowed us to cover almost all within- and between-cluster combinations in monkey R (3-3, 2-2, 2-3, 1-2). No electrode pair within cluster 1 reached this criterion. Clusters 1 and 3 were not recorded simultaneously. We found that the strength of GC connectivity varied as a function of electrode-pairing (**Fig. 4a, b, c**). Across all investigated frequencies, connectivity within cluster 3 was highest (n = 132 pairs), followed by connectivity within cluster 2 (n = 420) and between cluster 2 and 1 (n = 112). Connectivity between clusters 2 and 3 (n = 109) was low, however, suggesting a distinctive role for cluster 3 in the prefrontal working memory circuit matching its high within-cluster connectivity.

Second, we performed sliding-window analyses of spike-field locking within and between prefrontal clusters using MUA-LFP pairwise phase consistency (PPC). PPC quantifies the alignment of spikes in a ‘‘sender’’ electrode to specific phases of ongoing LFP oscillations in a ‘‘receiver’’ electrode, which is indicative of directed synaptic influences (Jacob et al., 2018; Liebe et al., 2012; Pesaran et al., 2008; Salazar et al., 2012; Siegel et al., 2009). As expected, within-cluster PPC was higher than between-

cluster PPC (**Fig. 4d, e, f**). PPC within clusters 2 and 3 showed different temporal dynamics and frequency-dependencies (cluster 2: n = 508 electrode pairs; cluster 3: n = 184): spike-field locking in cluster 2 was strongest in the memory delays and in the delta band (2 – 4 Hz), whereas spike-field locking in cluster 3 was most prominent in the theta band (4 – 8 Hz) and more persistent, peaking in particular in the second memory delay preceding the test (**Fig. 4d**). PPC between clusters 2 and 1 dominated in the delta band and in the memory delays (2→1: n = 330; 1→2: n = 294; **Fig. 4e**). In good agreement with our LFP-LFP connectivity results, spike-field locking was weak between clusters 2 and 3 (2→3: n = 222; 3→2: n = 264; **Fig. 4f**).

Third, we extended the analyses to investigate long-range frontoparietal connectivity (**Fig. 4g – l**). Block-wise conditional LFP-LFP Granger Causality was calculated for simultaneously recorded PFC-VIP electrode pairs. This method isolates the direct drive of one PFC cluster onto VIP, free from intermediate effects of other clusters (Chen et al., 2006). In line with previous findings (Jacob et al., 2018), PFC-to-VIP connectivity in monkey R was dominated by lower frequencies (delta and theta band), while VIP-to-PFC connectivity was also strong in the beta frequency band (16 – 32 Hz; **Fig. 4g, h**). Remarkably, while the strength of parieto-frontal beta band communication was similar for all prefrontal clusters (n = 94 pairs), cross-regional communication in the delta and theta band was cluster-specific and strongest for PFC cluster 3 (n = 19), followed by cluster 2 (n = 47) and cluster 1 (n = 28; **Fig. 4i**). These results were confirmed by an analysis of spike-field locking (PPC), which showed bidirectional, graded and cluster-specific connectivity between prefrontal and parietal cortex (**Fig. 4j, k, l**). Connectivity with VIP was strongest for PFC cluster 3 (3→VIP: n = 472; VIP→3: n = 354), followed by cluster 2 (2→VIP: n = 1152; VIP→2: n = 1006) and cluster 1 (1→VIP: n = 544; VIP→1: n = 506). The spectrotemporal patterns for each pairing were very reminiscent of the respective clusters' local connectivity within PFC. Cluster 3, for example, was characterized by prominent, persistent communication with VIP in the theta-band that peaked in the second memory delay preceding the test (**Fig. 4l**).

As in monkey R, the clusters in monkey W clearly segregated by local and long-range connectivity, which was strongest in the beta frequency band and from parietal to prefrontal cortex in this animal (**Fig. S4**).

Functional role of prefrontal clusters in working memory processing

So far, our findings convergently suggested that the primate prefrontal cortical sheet is parcellated into mesoscale modules with distinct local prefrontal connectivity and communication to distant areas in the parietal cortex. We therefore hypothesized that the identified clusters have specialized roles in the encoding, maintenance and decoding of working memory, a central cognitive function of the frontoparietal association network.

In monkey R, MUA differed strongly between the three clusters (**Fig. 5a**). Activity in cluster 1 (n = 66 multi-units) and cluster 2 (n = 144) increased sharply in response to sensory stimulation (i.e., visual

presentation of the sample and distractor numerosities). Firing decayed quickly to baseline in cluster 1, before ramping up again prior to presentation of the next stimulus. In contrast, activity in cluster 2 remained elevated throughout the memory delays. Units in cluster 3 (n = 59) showed stable and persistent firing across the entire trial with no appreciable deflections after sensory inputs. Matching these distinct patterns in spiking activity, working memory content was processed differently in the three clusters (information about sample and distractor numerosities measured by sliding-window analysis of percent explained variance ω^2; **Fig. 5b, c**). Cluster 1 and cluster 2 represented the sample and the distractor with the same strength and dynamics, without reflecting their different behavioral relevance. Information was highest during numerosity encoding (sensory epochs), and peaked again in cluster 1, but not cluster 2, during numerosity decoding (late memory epochs). In contrast, numerosity information in cluster 3 was low following stimulus presentation, but increased markedly for the sample, but not for the distractor, in the second memory delay, in the sense of recovery of working memory after interference (Jacob & Nieder, 2014).

Next, we examined the LFP burst patterns (**Fig. 5d**). Gamma and beta bursting followed alternating, antagonistic time courses in all three clusters (Lundqvist et al., 2023; Lundqvist et al., 2018; Lundqvist et al., 2016). Gamma bursting patterns matched the clusters' spiking activity almost perfectly (compare **Fig. 5d** to **Fig. 5a**; see also **Fig. 2i**). The probability of gamma bursting scaled with sample and distractor numerosity. Remarkably, bursting in the sensory and memory epochs was modulated in opposing directions (**Fig. 5e, f**). Gamma bursts increased with numerosity during encoding (i.e., visual presentation of sample and distractor; see also **Fig. 2l**) but decreased with numerosity during memory maintenance and decoding. This finding provides support for the notion that oscillatory bursts do not constitute information coding entities *per se*, but instead reflect "on states" of neuronal populations in the local microcircuit that process sensory and memory information with distinct coding schemes.

Beta bursting was triggered in cluster 1 and cluster 2 by the onset and offset of visual stimuli (**Fig. 5d**). This sensory pattern was almost absent in cluster 3. Here, beta bursting increased strongly during memory recovery after interference. Unlike gamma, beta bursting scaled positively with numerosity in all epochs with no reversals (**Fig. 5g, h**).

Together, these results suggest that our recordings in monkey R covered three functionally distinct prefrontal subdivisions with roles in working memory encoding and decoding (cluster 1; mainly local, within-PFC connectivity); memory maintenance (cluster 2; both local and cross-regional connectivity to VIP); memory recovery after distraction (cluster 3; mainly cross-regional connectivity to VIP).

In monkey W, spiking activity and numerosity information were more sustained and persisted throughout the memory delays (**Fig. S5a, b, c**). As in monkey R, gamma bursting matched spiking well and showed tuning reversals in the course of the trial (**Fig. S5d, e, f**). The recording sites did not span a "recovery cluster". Beta burst patterns differentiated clearly between individual clusters, two of which also displayed a reversal in sample numerosity tuning during memory maintenance (**Fig. S5d, g, h**).

Behavioral relevance of oscillatory burst activity for working memory

Finally, we asked whether the cluster-specific microcircuit “on states” were systematically linked to the animals’ working memory performance. To compare trials with high and low bursting, we calculated the percentage of trial time covered by oscillatory bursting activity (burst occupancy; normalized by the standard deviation across the session) (Karvat et al., 2021). Burst occupancy fluctuated slowly throughout the session in cycles of 10 to 20 trials (approximately 2 to 3 minutes) (**Fig. 6a**). Notably, these fluctuations affected both PFC and VIP as well as gamma and beta bursts (**Fig. 6a**) and became stronger as the recording session progressed (**Fig. 6b**). In both areas and frequency bands, burst probability in trials with high burst occupancy was uniformly offset compared to trials with low burst occupancy, lacking preference for specific trial epochs (**Fig. 6c**). These findings suggest that the extent of oscillatory bursting in local networks was influenced by global cognitive factors (e.g., attentional and motivational engagement).

In monkey R, increased gamma bursting (high gamma burst occupancy) in correct trials was associated with faster reaction times (negative correlation between gamma occupancy and reaction time; **Fig. 6d**). This pattern was present across PFC clusters (with the exception of cluster 2) and in VIP. In contrast, increased beta bursting (high beta burst occupancy) was found in trials with slower reaction times (positive correlation; **Fig. 6d**). Gamma and beta bursting had opposing effects on response accuracy, with gamma generally facilitating and beta hindering correct performance (**Fig. 6e**). Across both analyses, these patterns were strongest in cluster 3 and VIP and more similar to each other than for any other cluster pair, providing further support for tight connectivity between these two cortical areas.

In monkey W, we observed the same opposing influences of gamma and beta bursting on task performance (**Fig. S6a, b**). Overall, PFC was a stronger determinant of trial outcome than VIP. In line with our clustering analysis (**Fig. S3**), the transitions between clusters in this animal were more gradual than in monkey R.

Discussion

Here, we report spatially continuous, stable clusters of recording sites in the primate lateral PFC that segregate by oscillatory network activity, functional connectivity, working memory processing stages and behavioral influence on mnemonic performance. These multiple lines of evidence suggest that the frontoparietal working memory network is modularly organized and structured not by the represented information, but instead by the cognitive control operations that execute on this information.

Anatomical studies have identified multiple subdivisions of the non-human primate lateral PFC (area 46) based on cytoarchitecture (Petrides & Pandya, 1999; Rapan et al., 2023). For example, the anterior section has bigger pyramidal neurons in layer III and layer IV compared to the posterior section; the dorsal part has a prominent layer II, while the ventral part has a prominent layer IV. Notably, cortico-cortical connections of the posterior section were shown to be more widely spread across the brain compared to those of the anterior section. Connections with posterior parietal cortex (e.g. lateral intraparietal cortex) were especially strong (Petrides & Pandya, 1984; Rapan et al., 2023). This is in good agreement with our finding of stronger frontoparietal connectivity in the posterior cluster in monkey R compared to the anterior clusters. Together, these observations argue that the functionally dissociated clusters we describe are rooted in the anatomical structure of the PFC and in the frontoparietal connectome, a notion that also aligns well with recent computational theories of structure in neuronal activity (Ostojic & Fusi, 2024).

We used LFPs to functionally parcellate the lateral PFC (**Fig. 3, Fig. S2, Fig. S3**). LFPs represent a particularly suitable extracellular signal component to explore links between network activity and network anatomy, e.g., local and long-range wiring motifs. Microscale single-unit measurements only pick up a small fraction of the spiking activity in the vicinity of the recording electrodes, generating a very incomplete picture of the full network activity. In addition, neuronal representations in PFC are typically sparse, i.e., only few neurons carry critical information, meaning that single-neuron recordings alone cannot provide the dense observations necessary to detect higher-order structures (Lin et al., 2023). In contrast, mesoscale LFPs sum across all electrical signals generated in the local neuronal circuitry (Buzsáki et al., 2012), thus providing complete network coverage. At the same time, with a spread of not more than a few hundred micrometers (Lindén et al., 2011), LFPs are sufficiently contained in space to locate sharp module boundaries.

Supporting the interdependence between anatomical structure and oscillatory neuronal activity, we found that LFP bursts displayed fixed spectrotemporal properties (**Fig. 2**) as well as task-epoch and stimulus invariant synchrony with local spiking activity (**Fig. S1**). Remarkably, spike-LFP-coupling not only reflected local prefrontal, but also long-range frontoparietal connectivity (**Fig. 2**). The observed recording site-specific spatiotemporal patterns of LFP bursts therefore likely result from the combination of network anatomy and external driving factors (Miller et al., 2018), such as sensory inputs (to cluster 1 or 2 in

monkey R, **Fig. 5**), remote communication (between cluster 3 and VIP, **Fig. 4**), or global cognitive states (slow session-wide fluctuations, **Fig. 6**).

LFP bursts in monkey W also displayed spatial patterns with different frequency-band and trial-epoch characteristics, but the modular organization appeared less hierarchical than in monkey R, instead showing smoother transitions between clusters in the sense of spatial gradients (**Fig. S3**). Remarkably, however, the clusters in monkey W were also clearly segregated by the strength of connectivity, at both local and long-range scales (**Fig. S4**). It is reasonable to assume that the difference in clustering between the two animals could have resulted from the difference in prefrontal recording locations (compare **Fig. 3** and **Fig. S3**). Additionally, inter-individual differences in local and distant connectivity could play a major role.

The organizational principle we identified in lateral PFC differs fundamentally from that of domain-specific cortices, which are internal mappings of either physical space (e.g., sensory and motor homunculus (Gordon et al., 2023; Humphries et al., 2010; Penfield & Boldrey, 1937)) or of information space (e.g., numerosity map in parietal cortex (Harvey et al., 2013)). In contrast, the PFC modules in our recording field did not differentiate between working memory items (information), since sample and distractor triggered similar burst responses and spiking activity (**Fig. 3, Fig. 5, Fig. S5**). Our results suggest instead that the individual modules had specific roles in the control of working memory content, i.e., the encoding, maintenance and retrieval of information. These distinct operations were clearly reflected in the burst patterns recorded in monkey R, where the mapping between numerosity and burst probability was not fixed but reversed at the transition from the sensory to the memory delay epochs (**Fig. 5**). They also matched the connectivity patterns well: numerosity encoding and decoding were strongest in the anterior cluster with the weakest connection to VIP, while the recovery of memorized information after interference was strongest in the posterior cluster with the strongest frontoparietal communication (**Fig. 4, Fig. 5**) (Jacob et al., 2018; Jacob & Nieder, 2014; Rapan et al., 2023). Overall, organization of the prefrontal cortical sheet by working memory control processes is in good agreement with the role of the domain-general PFC in top-down executive control and adaptive behavior (Hanganu-Opatz et al., 2023).

Spatially organized LFP dynamics in PFC were recently proposed as a neural mechanism to modulate the gain of individual items stored in working memory (“spatial computing”) (Lundqvist et al., 2023). These control signals were hypothesized to arise functionally in an anatomically homogeneous prefrontal neuronal population. Using a significantly broader recording field, we now show that these spatiotemporal spectral dynamics are in fact rooted in cortical anatomy. A pre-existing modular structure is engaged according to the operational demands of a given task. The modular architecture does not result from the cognitive operation *per se*. Depending on the nature of the task, individual prefrontal modules may appear separated by consecutive memory items when the primary operational demand is to keep an ordered list of items (as in serial working memory (Lundqvist et al., 2023)); or, as in the present case, the modules reflect the same memory item undergoing different processing stages in order to protect it from

interference. These observations are in fact two examples of the same principle, namely, modular organization by cognitive operations.

Acknowledgements

This work was supported by German Research Foundation (DFG) grants JA 1999/1-1 and JA 1999/6-1 to S.N.J and grants NI 618/10-1 and NI 618/13-1 to A.N. The funders had no role in study design, data collection and analysis, decision to publish or preparation of the manuscript.

Author contributions

S.N.J. and A.N. designed the experiments. S.N.J. collected the data. X.W. and D.H. performed data analysis. X.W. and S.N.J. wrote the manuscript with contributions from A.N.

Competing interests

The authors declare no competing interests.

Figures

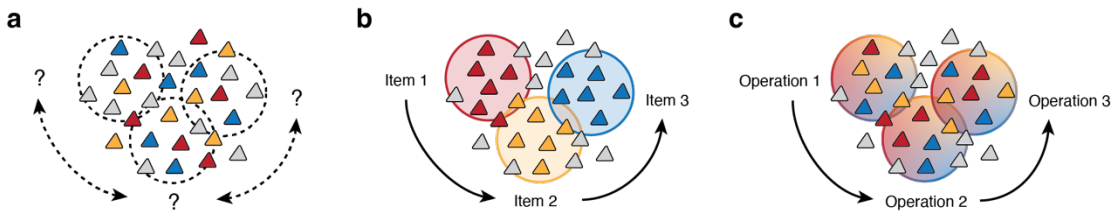

Fig. 1 | Hypothesized spatial and functional organization of prefrontal working memory representations. a, No organization. Individual neurons with different selectivities for memorized items are interspersed in a salt-and-pepper-like manner. There is no apparent spatial clustering or ordered temporal progression of activity. **b,** Organization by working memory content. Individual neurons are clustered by item selectivity. Activity travels systematically through the clusters, engaging each cluster whenever its associated item is processed. Individual neurons are, therefore, activated in multiple trial epochs (e.g., memory encoding, maintenance, and decoding). **c,** Organization by working memory operation. Individual neurons are clustered by the cognitive operation they are engaged in (e.g., memory encoding, maintenance or decoding). Activity travels systematically through the clusters, engaging subsets of neurons with different item selectivities within each cluster whenever its associated processing stage is reached. Individual neurons are, therefore, activated mainly in a single trial epoch.

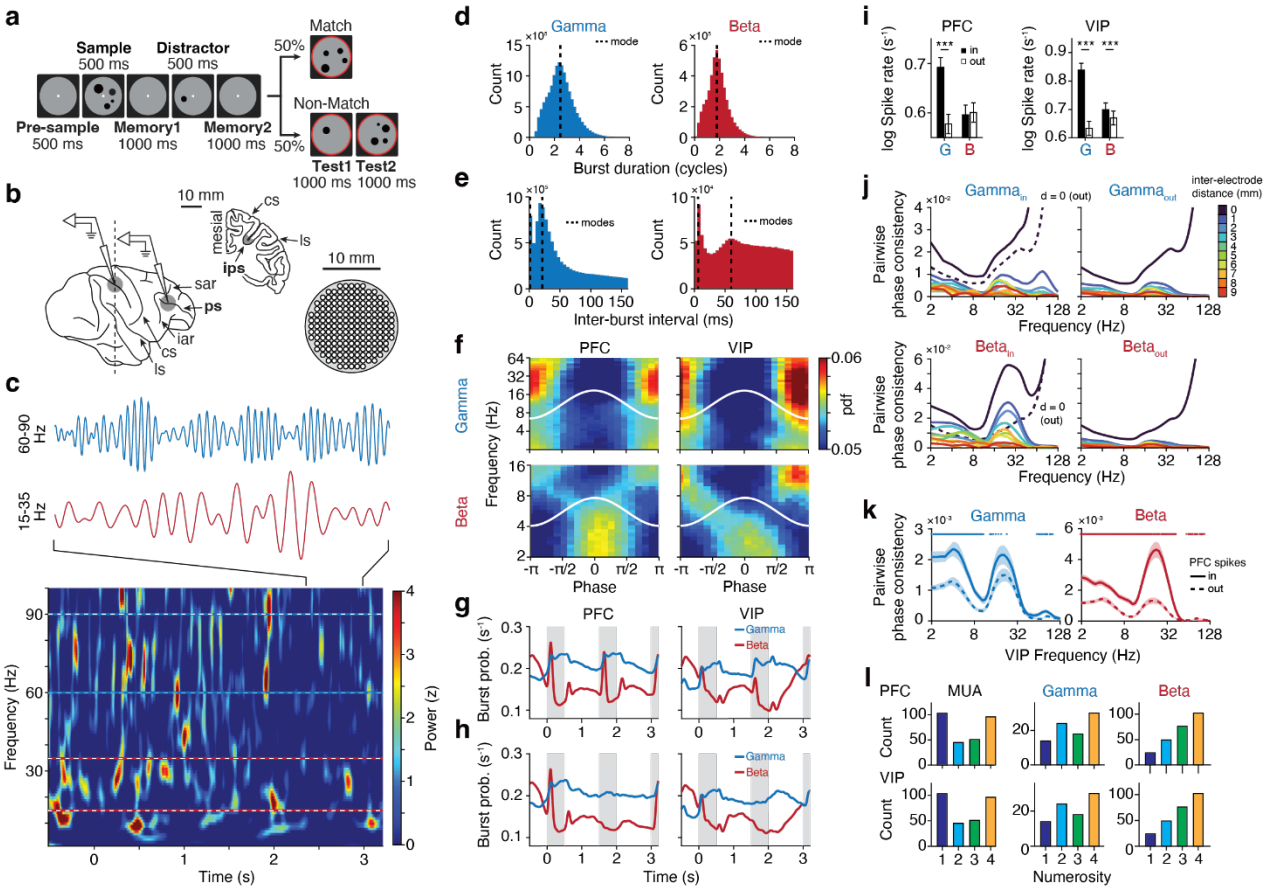

Fig. 2 | Working memory related oscillatory burst activity. a, Delayed-match-to-numerosity task. Two monkeys indicated whether a test stimulus contained the same number of dots (numerosity) as the memorized sample. A task-irrelevant distractor was presented during the memory delay. **b,** Schematic of extracellular recordings. In each session, four pairs of microelectrodes were inserted through grids into the lateral PFC and into the fundus of the intraparietal sulcus (ips; inset) in VIP. ps, principal sulcus; sar, superior arcuate sulcus; iar, inferior arcuate sulcus; cs, central sulcus; ls, lateral sulcus. **c,** Top, example LFP traces, band-pass filtered in the gamma (60 – 90 Hz) and beta (15 – 35 Hz) frequency range. Bottom, spectrogram of LFP activity (normalized to average band power taking together 9 previous trials and the current trial) recorded in an example trial in PFC. **d,** LFP burst duration at full-width-half-maximum (FWHM) of the 2D Gaussian kernels fitted to each individual burst. Data from all trial epochs were pooled across monkeys and electrodes (n = 1230). The mode is marked. **e,** Inter-burst interval, defined as the temporal delay between peaks of two subsequent bursts within each band. The modes are marked. **f,** Top, phase coupling of gamma burst peaks to ongoing LFP oscillations in PFC (left) and VIP (right). Phase 0 corresponds to the peak, while phase ±π corresponds to the trough of the LFP oscillation (white lines). Bottom, same for beta bursts. **g,** Trial-averaged burst probabilities in the gamma and beta frequency ranges in PFC (left; n = 616 electrodes) and VIP (right; n = 614 electrodes) in correct trials with a distractor. **h,** Same as **g** for trials without a distractor. **i,** Left, spike rate (multi-unit activity) inside and outside of gamma

and beta LFP bursts (left and right respectively) in PFC. Right, same for VIP. Spike rate follows normal distribution after transformed to the logarithmic scale (Kolmogorov-Smirnov test with $p < 0.05$). Paired t-Test. ***, $p < 0.001$. **j,** Top, within-electrode ($d = 0$ mm) and inter-electrode ($d = 1 – 9$ mm) spike-field locking measured by pairwise phase consistency (PPC) for spikes inside (left) and outside (right) of gamma LFP bursts in PFC. The within-electrode PPC of outside-burst spikes is duplicated on the left for comparison (dashed line). Bottom, same for beta LFP bursts. **k,** Cross-regional PPC, quantified by the alignment of PFC spikes inside and outside of LFP bursts to simultaneously recorded VIP oscillations for gamma (left) and beta LFP bursts (right). Data were pooled across all electrode pairs. Wilcoxon signed-rank test. Thin bar, $p < 0.05$; thick bar, $p < 0.01$. **l,** Top, count of PFC electrodes with significant tuning of multi-unit spiking activity (left), gamma (middle) or beta LFP burst activity (right) to the sample numerosity in the sample epoch, split by numerosity eliciting peak MUA activity or burst probability. Bottom, same for VIP.

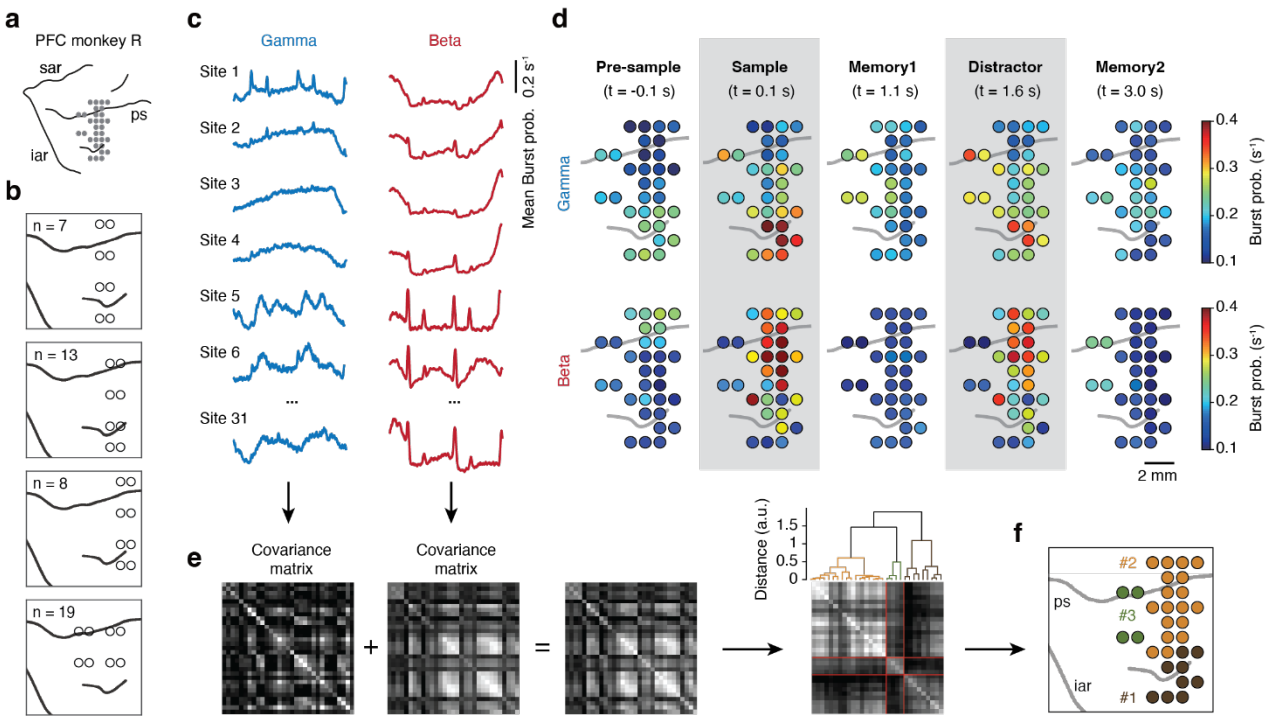

Fig. 3 | Spatial clustering of prefrontal recording sites by burst probability. a, Spatial layout of recording sites in PFC of monkey R, pooled across all sessions. The electrode penetration sites are displayed over the reconstructed cortical surface. **b,** Distinct recording layouts with the number of sessions the respective layouts were used. **c,** Burst probability at each recording site (n = 31 total) averaged across all correct trials in the gamma (left) and beta frequency range (right). **d,** Spatial distribution of trial-averaged burst probability at selected time points during the trial. **e,** Analysis pipeline for spatial clustering of recording sites by similarity in burst activity. Covariance matrices for gamma and beta burst probabilities were computed for each trial condition (4 sample numerosities × 4 distractor numerosities) and then summed. The resulting covariance matrix was submitted to hierarchical agglomerative clustering. **f,** Spatial layout of clustered recording sites in PFC of monkey R.

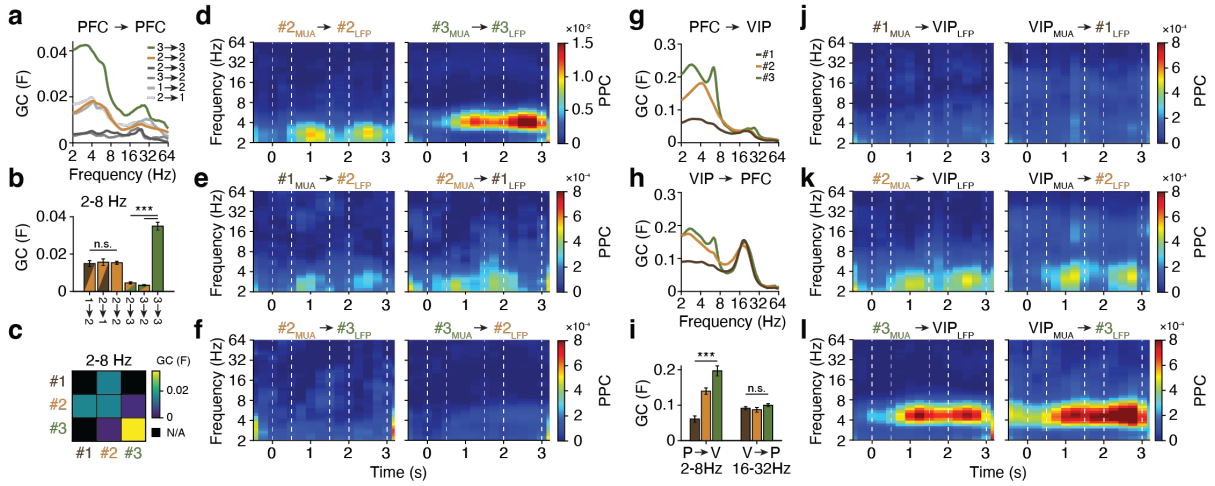

Fig. 4 | Prefrontal cluster-specific local and long-range connectivity. a, LFP-LFP Granger Causality (GC) within and between PFC clusters of monkey R. Analysis was performed using equidistant electrode pairs of 3 to 4 mm distance. **b,** LFP-LFP GC within and between PFC clusters of monkey R in the 2 – 8 Hz frequency range. Wilcoxon rank sum test. ***, $p < 0.001$. **c**, Same as **b** displayed in matrix form. Electrode pairs of 3 to 4 mm distance were not recorded for all cluster combinations. **d,** Spike-field locking within PFC clusters 2 and 3 of monkey R, measured by MUA-LFP pairwise phase consistency (PPC), for electrode pairs of 3 to 4 mm distance. **e**, Same as **d** between clusters 1 and 2. **f**, Same as **f** between clusters 2 and 3. **g,** LFP-LFP fronto-parietal GC between PFC electrode clusters and pooled VIP electrodes of monkey R. **h,** LFP-LFP parieto-frontal GC between pooled VIP electrodes and PFC electrode clusters of monkey R. **i**, LFP-LFP fronto-parietal GC in the 2 – 8 Hz frequency range (left) and LFP-LFP parieto-frontal GC in the 16 – 32 Hz frequency range (right) of monkey R. Kruskal-Wallis test. ***, $p < 0.001$; n.s., not significant. **j,** Bidirectional MUA-LFP spike-field locking (PPC) between PFC cluster 1 electrodes and pooled VIP electrodes of monkey R. **k**, Same as **j** between PFC cluster 2 electrodes and VIP. **l**, Same as **j** between PFC cluster 3 electrodes and VIP.

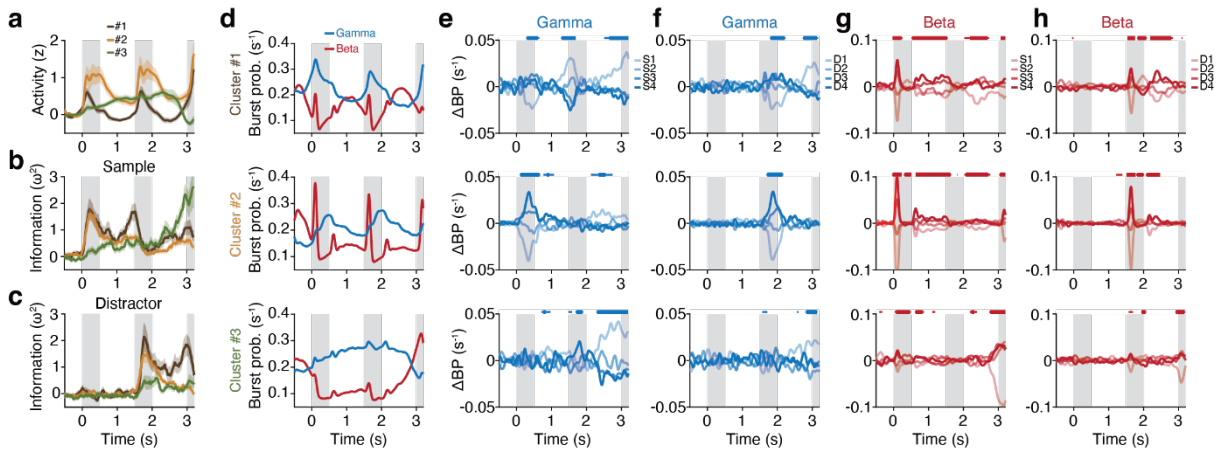

Fig. 5 | Prefrontal cluster-specific burst activity and neuronal selectivity. a, Neuronal activity (MUA, normalized to fixation epoch) for the three PFC clusters in monkey R. **b,** Neuronal selectivity (MUA) for sample numerosity, measured by ω^2 percent explained variance, for the three PFC clusters in monkey R. **c,** Same as **b** for distractor numerosity. **d,** Trial-averaged burst probabilities (correct trials) in the gamma and beta frequency ranges for the three PFC clusters in monkey R. **e,** Detrended burst probabilities in the gamma frequency range for each sample numerosity and PFC cluster in monkey R. Repeated measures ANOVA. Thin bar, $p < 0.05$; thick bar, $p < 0.01$. **f,** Same as **e** for distractor numerosity. **g,** Same as **e** for the beta frequency range. **h,** Same as **g** for distractor numerosity.

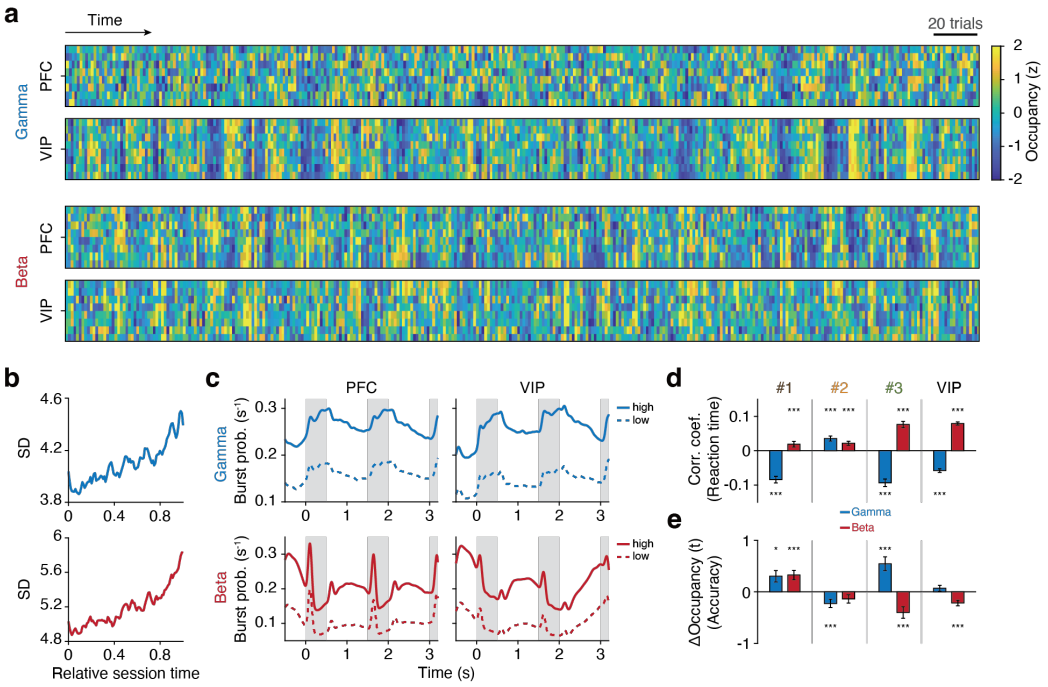

Fig. 6 | Global fluctuations in burst activity and relationship to behavioral performance. a, Trial-wise burst occupancy (all trials), measured as the percentage of trial time covered by oscillatory bursting activity (normalized by standard deviation across the session), in one representative session of monkey R. Each region contains 8 simultaneously recorded electrodes, aligned in rows. **b,** Temporal evolution of burst occupancy fluctuation (standard deviation) across session time, averaged across animals, brain regions and sessions. **c,** Top, trial-averaged burst probability in the gamma frequency range in trials with high and low occupancy (median split; solid and dashed lines, respectively) for pooled PFC and VIP electrodes (left and right, respectively) across animals and sessions. Bottom, same for the beta frequency range. **d,** Median trial-wise correlation coefficient (Pearson) between burst occupancy in the gamma and beta frequency ranges and the reaction time in correct trials of monkey R. Data are displayed for each PFC cluster and for pooled VIP electrodes. Error bars, s.e.m. across electrodes. Paired t-Test. ***, $p < 0.001$. **e,** Difference in burst occupancy between correct and error trials of monkey R. Error bars, s.e.m. across electrodes. Paired t-Test. *, $p < 0.05$; ***, $p < 0.001$

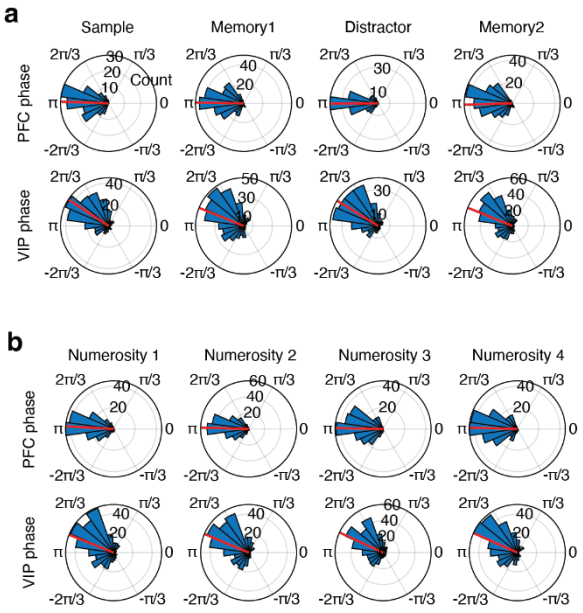

Fig. S1 | Phase coupling of gamma bursts to beta oscillations. a, Top row, distribution of preferred phases for PFC electrodes (radius: electrode count) with significant phase coupling of gamma burst peaks to ongoing beta oscillations (at 29 Hz), determined for each trial epoch separately. The mean phase is marked (red line). Bottom row, same for VIP electrodes. **b,** Top row, distribution of preferred phases for PFC electrodes (radius: electrode count) with significant phase coupling of gamma burst peaks to ongoing beta oscillations (at 29 Hz) during the sample epoch, split by sample numerosity. The mean phase is marked (red line). Bottom row, same for VIP electrodes.

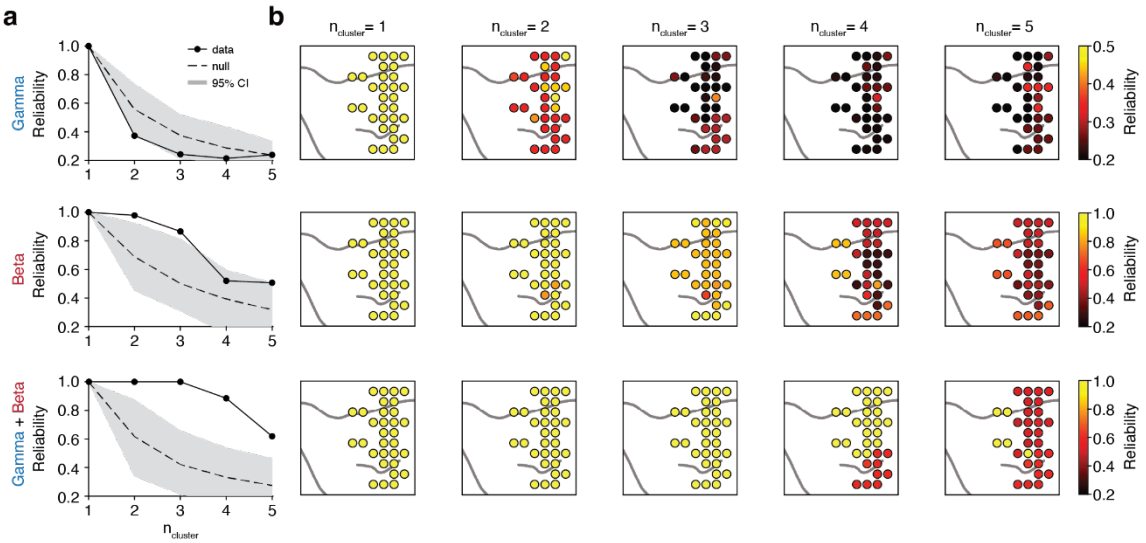

Fig. S2 | Reliability of spatial clustering of prefrontal recording sites in monkey R. a, Top, gamma burst probability covariance matrices were calculated using 100 random split-halves (trial subsampling at each PFC recording site) and submitted to hierarchical agglomerative clustering (see Fig. 3e). Clustering reliability is measured as the percentage of recording sites consistently assigned to the same cluster and shown as a function of the number of selected clusters. The mean (dashed line) and 95% confidence interval (CI, shaded area) of the clustering reliability null distribution are shown. Middle, same for beta burst probability covariance. Bottom, same for combined gamma and beta probability covariance. **b,** Clustering reliability by recording site.

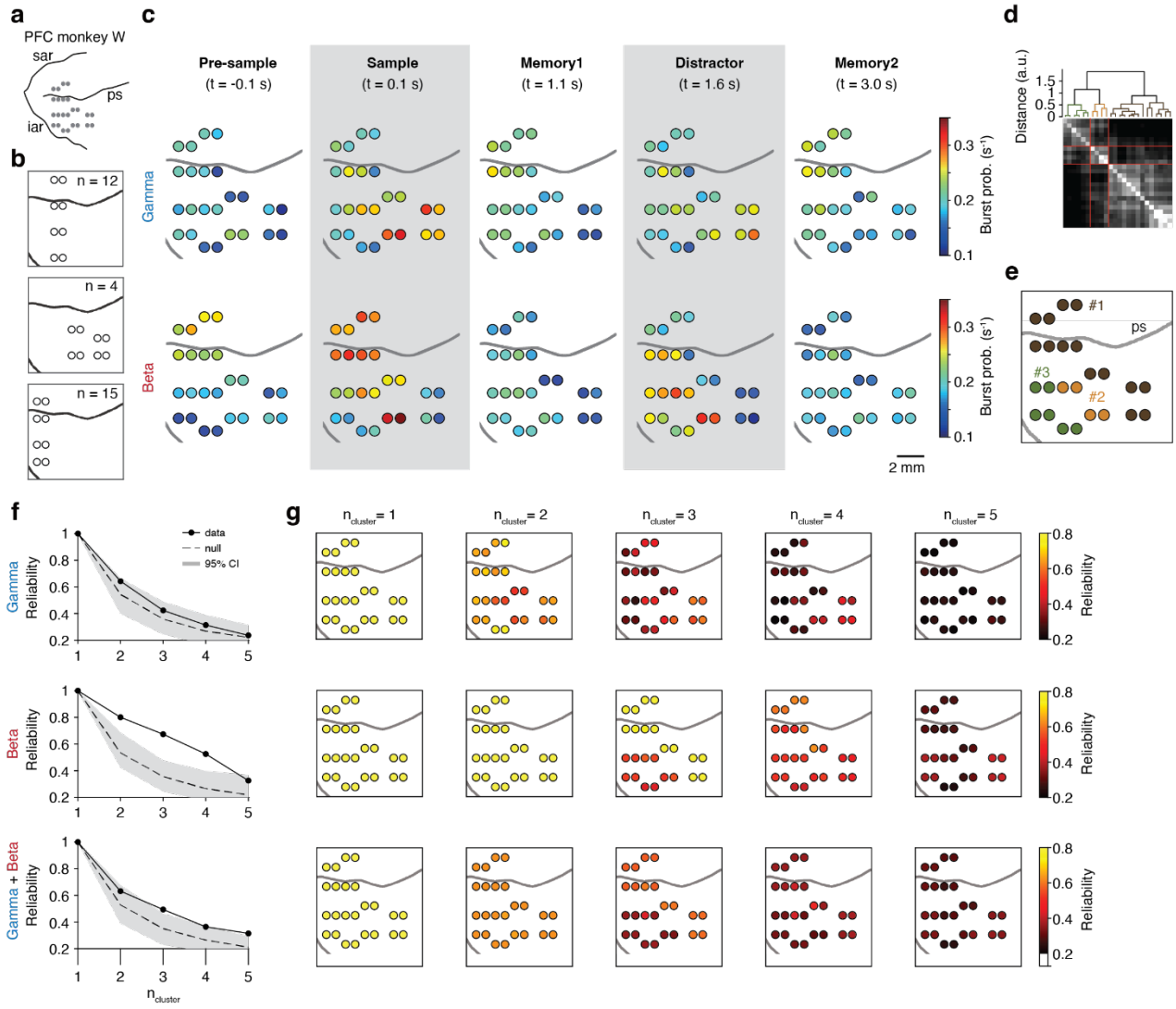

Fig. S3 | Spatial clustering of prefrontal recording sites by burst probability in monkey W. a, Spatial layout of recording sites in PFC of monkey W, pooled across all sessions. The electrode penetration sites are displayed over the reconstructed cortical surface. **b,** Distinct recording layouts with the number of sessions the respective layouts were used. **c,** Spatial distribution of trial-averaged burst probability at selected time points during the trial. **d,** Hierarchical agglomerative clustering of the summed covariance matrices for gamma and beta burst probabilities (see Fig. 3e). **e,** Spatial layout of clustered recording sites. **f,** Top, gamma burst probability covariance matrices were calculated using 100 random split-halves (trial subsampling at each PFC recording site) and submitted to hierarchical agglomerative clustering. Clustering reliability is measured as the percentage of recording sites consistently assigned to the same cluster and shown as a function of the number of selected clusters. The mean (dashed line) and 95% confidence interval (CI, shaded area) of the clustering reliability null distribution are shown. Middle, same for beta burst probability covariance. Bottom, same for combined gamma and beta probability covariance. **b,** Clustering reliability by recording site.

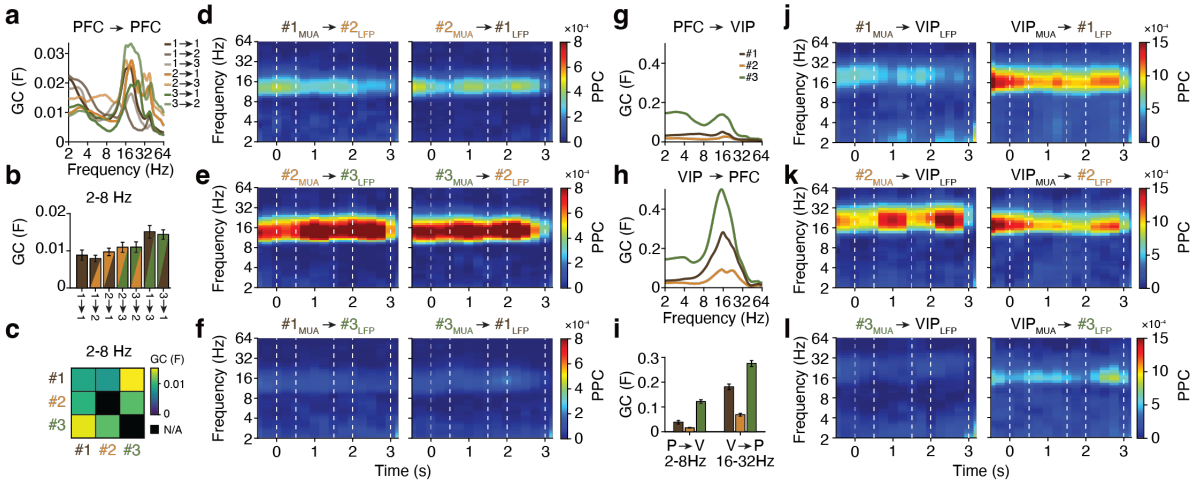

Fig. S4 | Prefrontal cluster-specific local and long-range connectivity in monkey W. a, LFP-LFP Granger Causality (GC) within and between PFC clusters of monkey W. Analysis was performed using equidistant electrode pairs of 3 to 4 mm distance. **b,** LFP-LFP GC within and between PFC clusters in the 2 – 8 Hz frequency range. Wilcoxon rank sum test. ***, $p < 0.001$. **c**, Same as **b** displayed as confusion matrix. Electrode pairs of 3 to 4 mm distance were not recorded for all cluster combinations. **d,** Spike-field locking between PFC clusters 1 and 2, measured by MUA-LFP pairwise phase consistency (PPC), for electrode pairs of 3 to 4 mm distance. **e**, Same as **d** between clusters 2 and 3. **f**, Same as **f** between clusters 1 and 3. **g,** LFP-LFP fronto-parietal GC between PFC electrode clusters and pooled VIP electrodes. **h,** LFP-LFP parieto-frontal GC between pooled VIP electrodes and PFC electrode clusters. **i**, LFP-LFP fronto-parietal GC in the 2 – 8 Hz frequency range (left) and LFP-LFP parieto-frontal GC in the 16 – 32 Hz frequency range (right). Wilcoxon rank sum test. ***, $p < 0.001$; n.s., not significant. **j,** Bidirectional MUA-LFP spike-field locking (PPC) between PFC cluster 1 electrodes and pooled VIP electrodes. **k**, Same as **j** between PFC cluster 2 electrodes and VIP. **l**, Same as **j** between PFC cluster 3 electrodes and VIP.

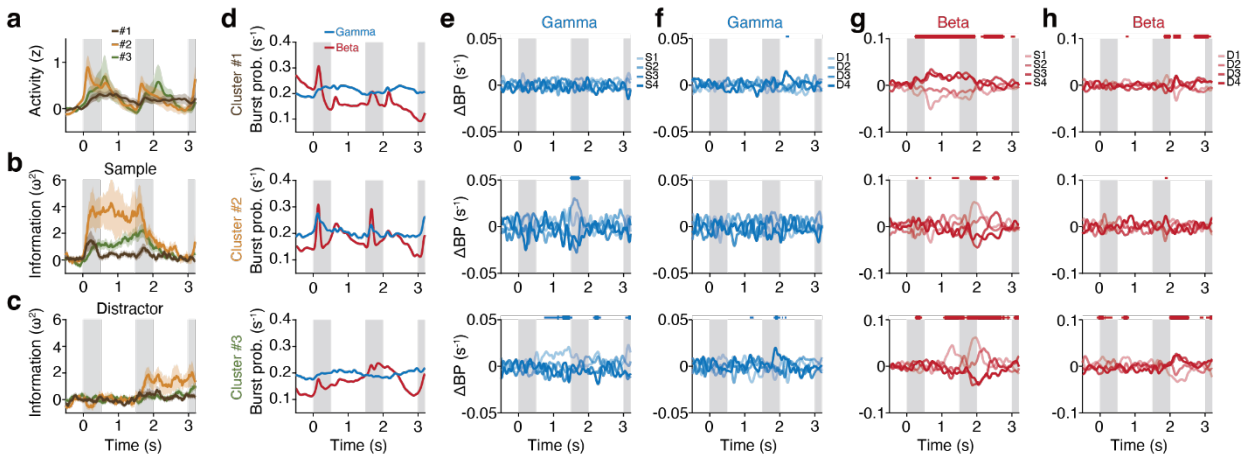

Fig. S5 | Prefrontal cluster-specific burst activity and neuronal selectivity in monkey W. a, Neuronal activity (MUA, normalized to fixation epoch) for the three PFC clusters in monkey W. **b,** Neuronal selectivity (MUA) for sample numerosity, measured by ω^2 percent explained variance, for the three PFC clusters. **c,** Same as **b** for distractor numerosity. **d,** Trial-averaged burst probabilities (correct trials) in the gamma and beta frequency ranges for the three PFC clusters. **e,** Detrended burst probabilities in the gamma frequency range for each sample numerosity and PFC cluster. Repeated measures ANOVA. Thin bar, $p < 0.05$; thick bar, $p < 0.01$. **f,** Same as **e** for distractor numerosity. **g,** Same as **e** for the beta frequency range. **h,** Same as **g** for distractor numerosity.

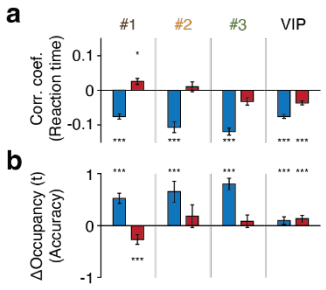

Fig. S6 | Behavioral relevance of oscillatory bursting activity in monkey W. a, Median trial-wise correlation coefficient (Pearson) between burst occupancy in the gamma and beta frequency ranges and the reaction time in correct trials of monkey W. Data are displayed for each PFC cluster and for pooled VIP electrodes. Error bars, s.e.m. across electrodes. Paired t-Test. ***, $p < 0.001$. **e,** Difference in burst occupancy between correct and error trials of monkey W. Error bars, s.e.m. across electrodes. Paired t-Test. **, $p < 0.01$; ***, $p < 0.001$

Methods

Subjects

Two adult male rhesus monkeys (*Macaca mulatta*, 12 and 13 years old) were used for this study and implanted with two right-hemispheric recording chambers (14 mm diameter) centered over the principal sulcus of the lateral prefrontal cortex (PFC) and the ventral intraparietal area (VIP) in the fundus of the IPS (Jacob et al., 2018; Jacob & Nieder, 2014). All experimental procedures were conducted in accordance with the guidelines for animal experimentation approved by the local authority at the Regierungspräsidium Tübingen.

Task and stimuli

The monkeys grabbed a bar to initiate a trial. Eye fixation was enforced within 1.75 ° visual angle to a central white dot (ISCAN, Woburn, MA). Stimuli were presented on a centrally placed gray circular background subtending 5.40 ° of visual angle. Following a 500 ms pre-sample (fixation only) period, a 500 ms sample stimulus containing one to four dots was shown. The monkeys had to memorize the sample numerosity for 2,500 ms and compare it to the number of dots (one to four) presented in a 1,000 ms test stimulus. Test stimuli were marked by a red ring surrounding the circular background. If the numerosities matched (50 % of trials), the animals released the bar (correct match trial). If the numerosities were different (50 % of trials), the animals continued to hold the bar until the matching number was presented in the subsequent image (correct nonmatch trial). Match and nonmatch trials were pseudorandomly intermixed. Correct trials were rewarded with a drop of water. In 80 % of trials, a 500 ms distractor numerosity of equal numerical range was presented between the sample and test stimulus. The distractor numerosity was not systematically related to either the sample or test numerosity and therefore was not required to solve the task. In 20 % of trials, a 500 ms gray background circle without dots was presented instead of an interfering stimulus (control condition, blank). Trials with and without distractors were pseudorandomly intermixed. Stimulus presentation was balanced; a given sample was followed by all interfering numerosities with equal frequency, and vice versa.

Low-level, non-numerical visual features could not systematically influence task performance (Nieder et al., 2002): in half of the trials, dot diameters were selected at random. In the other half, dot density and total occupied area were equated across stimuli. CORTEX software (NIMH, Bethesda, MD) was used for experimental control and behavioral data acquisition. New stimuli were generated before each recording session to ensure that the animals did not memorize stimulus sequences.

Electrophysiology

In each recording session, four pairs of 1 MΩ glass-isolated single-contact tungsten microelectrodes were acutely inserted into the prefrontal and parietal chambers through grids with 1 mm inter-electrode spacing. The selection of insertion sites (electrode layouts) changed repeatedly. Between 4 to 19 recording sessions were obtained with each layout. In PFC, 4 different electrode layouts were used for monkey R, and 3 layouts for monkey W (covering up to 6 mm x 10 mm and 9 mm x 10 mm, respectively). To reach VIP, electrodes were passed along the intraparietal sulcus to a depth of 9 to 13 mm below the cortical surface. Prior to recording neuronal activity in VIP, proper positioning of the electrodes was ensured by physiological criteria (response to tactile and moving visual stimulation). Electrodes were advanced until spiking activity was detected. No attempt was made to target a certain cortical layer. Signal acquisition, amplification, filtering, and digitalization were performed with the MAP system (Plexon, Dallas, TX). Extracellular voltages were recorded with unity-gain headstages and hardware bandpass-filtering to separate spiking activity (100 – 8000 Hz, sampling rate 40 kHz) from local field potentials (LFP; 0.7 – 170 Hz, sampling rate 1 kHz).

Data analysis

Analysis was performed with MATLAB (Mathworks, Natick, MA) using customized scripts, the FieldTrip toolbox (Oostenveld et al., 2011) and the CircStat toolbox (Berens, 2009).

LFP burst extraction

Power-line noise was removed with a 4th-order Butterworth notch filter at 50 Hz, along with its first and second harmonics. Transient bursting events were extracted from the LFP spectrogram of each trial. The raw LFP signals were trial-segmented and time-frequency transformed with additive adaptive superlets as implemented by the Superlet method (Moca et al., 2021). Superlet uses the geometrical mean of spectral power estimated with a set of Morlet wavelets with increasingly constrained bandwidth, which enables super-resolution in both the time and frequency domain. The base wavelet had a temporal spread of 3 cycles. The order (number of wavelets) was linearly defined based on the frequencies of interest, ranging from 3 to 30. The frequency range of interest was set at 2 to 128 Hz with a linear stepping of 1 Hz. Trials were padded with 1000 ms at the beginning and at the end. Spectrograms were estimated with a temporal resolution of 1 ms.

To remove slow-trend linear noise (e.g., residual power line noise) and pink (1/f) background noise, the power spectrogram of each trial was normalized to the average spectral power of 9 previous trials and the current trial. LFP bursts were identified as intervals when the instantaneous spectral power exceeded 2 standard deviations (SD) above the mean. The Watershed algorithm was used to separate neighboring

bursts. 2D tilted Gaussian kernels were fitted to the local power spectrogram for each of these burst candidates, centered at the local maximum (Lundqvist et al., 2016). The frequency center, frequency spread, temporal center, temporal spread and the frequency modulation angle were fitted for each Gaussian kernel (i.e., individual burst). The temporal duration (lifetime) of an LFP burst was defined by the full-width-at-half-maximum (FWHM) of each fitted Gaussian kernel. The inter-burst interval was defined as the temporal distance between peak power in each consecutive pair of bursts in the same frequency band within the same electrode. Bursts of short length (< 1 cycle), small frequency spread (< 1 SD) or with saturated LFP signals were excluded from further analysis.

Burst-field coupling

Burst-field coupling was determined using the time of peak power in relation to the phases (n = 20 phase bins) of ongoing lower-frequency oscillations. Phases were estimated by convolving the LFP with frequency-dependent Hanning-windowed complex sinusoids (logarithmic frequencies from 2 to 128 Hz, kernel width of 3 cycles) after removing phase-locked event related potentials (ERPs). To compare the phase locking of LFP bursts in each task epoch and across each numerosity condition, the phase coherency at the target frequency was estimated with the complex average M across n samples:

$$M = \frac{1}{n}\sum_{k=1}^{n} e^{i\varphi_k}$$

The preferred phase was represented by the argument of complex average M. Statistical testing was performed for each electrode by comparing the mean vector length $|M|$ with a null distribution created by randomly shuffling the association of single-trial spike trains and corresponding LFP traces (n = 1000 repetitions, $p < 0.05$).

Burst probability

For each frequency band, the probability of burst occurrence at each time point was estimated with incidence-accumulation: the time interval covered by each burst was transformed into a binary step function, which was summed and averaged across trials. Trial numbers were balanced for all sample and distractor numerosities by stratifying to the smallest number of correct trials across all conditions. The stratification was repeated 25 times, and the mean burst probability was calculated. The time course of burst probabilities was then smoothed with a 150 ms Gaussian window for visualization.

Sensory-triggered beta bursts were considered present if the beta burst probability during the first 200 ms after sample and distractor numerosity presentation exceeded 2 SD above the mean across the entire trial for at least 10 ms.

To quantify the modulation of burst probability by numerosity, a sliding window ANOVA (200 ms width, 20 ms steps) was performed for each sample and distractor numerosity.

Multi-unit activity

To separate multi-unit activity (MUA) from noise, we fitted a Gaussian mixture model to the probability density function of all recorded threshold crossing amplitudes at each electrode using:

$$p(x) = \sum_{i=1}^{k} p_i \Phi_i(x)$$

$$\Phi_i(x) = \frac{1}{\sqrt{2\pi {\sigma_i}^2}} e^{-\frac{(x-\mu_i)^2}{2{\sigma_i}^2}}$$

The fitting of parameters p_i, μ_i, σ_i was achieved by maximizing the posterior probability of each data point belonging to its assigned cluster. The number of components k was fitted using goodness of fit (Akaike information criterion, AIC). The Gaussian component with the smallest amplitude was taken as the noise distribution. All spikes with amplitudes exceeding 1.96 SD above the mean of the noise distribution were taken as MUA. Electrodes with MUA were included in further analysis if the average spike rate across trials was larger than 1 spike/s and the spike rate was significantly modulated during the trial (one-way ANOVA across pre-sample, sample, first memory, distractor, and second memory epoch; evaluated at $p < 0.05$).

MUA spike rate inside and outside of bursts was calculated using

$$r_{in} = \frac{n_{in}}{t_{burst}};\ r_{out} = \frac{n_{out}}{t_{all} - t_{burst}}$$

where n_{in} and n_{out} are the number of spikes inside and outside of bursts, t_{burst} is the lifetime of the burst and t_{all} is the trial length. MUA spike rates were then transformed to logarithmic scale to obtain a normal distribution for statistical testing.

Spike-field locking

Spike field locking was measured using the instantaneous LFP phase at each spike time. To estimate the instantaneous phase of each spike, a 1 s LFP segment centered around each spike was convolved with frequency-dependent Hanning-windowed complex sinusoids (logarithmic frequencies from 2 to 128 Hz, kernel width of 3 cycles). The instantaneous phase φ of each spike is the argument of the complex Fourier coefficients. Pairwise phase consistency (Vinck et al., 2010) was determined using:

$$ppc = \frac{(\sum_{k=1}^{n} \cos(\varphi_k))^2 + (\sum_{k=1}^{n} \sin(\varphi_k))^2 - n}{n(n-1)}$$

where n is the number of observations (i.e., spikes). For time-resolved analyses, we used a sliding window of 500 ms width and 250 ms steps.

Neuronal information

To quantify the information about the sample or distractor numerosity carried by MUA or burst probability, we calculated the percentage of explained variance (ω^2 PEV) (Buschman et al., 2011) using

$$\omega^2 \text{ PEV } = \frac{SS_{group} - df \times MSE}{SS_{all} + MSE}$$

where df is the degrees of freedom, MSE is the mean squared error and SS is the sum of squares (all from ANOVA). Sample and distractor PEV were calculated independently for each electrode with a sliding window of 200 ms width and 20 ms steps.

Spatial clustering of LFP burst patterns

The similarity of LFP burst patterns was determined by agglomerative hierarchical clustering as implemented in MATLAB. Burst probability covariances were calculated for each recording site pair using the mean gamma and beta burst probability at each site across all recording sessions and assembled into covariance matrices. Trial numbers were balanced for all sample and distractor numerosities as described above. The clustering algorithm then iteratively merged sites with higher covariance together, until all sites were grouped into a single cluster. This resulted in a tree-structured representation (dendrogram) of the covariance matrix. By descending the dendrogram and cutting the tree at each node, the covariance structure was separated into maximally n non-overlapping clusters (i.e., branches).

We determined the optimal number of clusters n based on split-half reliability. Each session was randomly split into two halves after balancing the number of trials for each numerosity. The clustering algorithm was run independently on each of the split-halves and terminated at varying numbers of clusters (n = 1 to 5). Cluster labeling (assignment) was then compared between each pair of split-halves. This process was repeated 100 times, and the proportion of sites labelled consistently across split-halves was considered as the clustering reliability. To determine statistical significance, we generated a null distribution by shuffling across recording sites 10 times for each split-half, leading to 1000 (100 x 10) samples.

Granger causality

We calculated bivariate Granger causality (Granger, 1969) as implemented in Fieldtrip using

$$GC_{x\to y(\omega)} = \ln\left(\frac{pow_y(\omega)}{pow_y(\omega) - \left(\Sigma_{xx} - \frac{\Sigma_{yx}^2}{\Sigma_{yy}}\right)\left|H_{yx}(\omega)\right|^2}\right)$$

where $GC_{x\to y(\omega)}$ is the Granger causality from signal x to signal y at frequency ω, $pow_y(\omega)$ is the power of signal y at frequency ω, Σ_{xx} and Σ_{yy} are the noise variances of signal x and y, Σ_{yx} is the noise covariance in the auto-regressive model between signal x and y, and $H_{yx}(\omega)$ is the spectral transfer matrix.

For block-wise conditional Granger causality (Chen et al., 2006) between PFC clusters and VIP, we used

$$GC_{x\to y|[xy](\omega)} = \ln\frac{\mathrm{var}(\varepsilon'_{y,t})}{\mathrm{var}(\varepsilon_{y,t})}$$

where $\varepsilon'_{y,t}$ is the residual of the reduced autoregressive model predicting y with history of all other variables except of x, and $\varepsilon_{y,t}$ is the residual of the full vector model including x. We grouped PFC electrodes by the cluster they were assigned to and calculated the GC between each pair of simultaneously recorded clusters in each session.

Burst occupancy

We defined the proportion of trial time covered by bursts as the burst occupancy (OCP) of a trial (Seedat et al., 2020) using

$$OCP = \frac{nt_{burst}}{nt_{all}}$$

where nt_{burst} is the number of time points covered by burst and nt_{all} is the overall number of time points across the whole trial. OCP standard deviation was calculated with a sliding window of 20 trials width and varying step size depending on the length of the session (n = 100 steps).

The correlation between OCP and task accuracy was calculated by comparing the OCP between correct and error trials using a paired t-Test. The resulting t-statistic of each electrode was used to index the strength of the correlation. The correlation between OCP and reaction time was calculated using Pearson correlation, including only correct match trials. The correlation coefficient of each electrode was used to index the strength of the correlation.

Data availability

Raw data are available on request from the authors. Source data are provided with this paper.

Code availability

Code is available on request from the authors.

References

Aoi, M. C., Mante, V., & Pillow, J. W. (2020). Prefrontal cortex exhibits multidimensional dynamic encoding during decision-making. *Nature Neuroscience*, *23*(11), 1410-1420. https://doi.org/10.1038/s41593-020-0696-5

Badre, D., & D'Esposito, M. (2007). Functional Magnetic Resonance Imaging Evidence for a Hierarchical Organization of the Prefrontal Cortex. *Journal of Cognitive Neuroscience*, *19*(12), 2082-2099. https://doi.org/10.1162/jocn.2007.19.12.2082

Badre, D., & D'Esposito, M. (2009). Is the rostro-caudal axis of the frontal lobe hierarchical? *Nature Reviews Neuroscience*, *10*(9), 659-669. https://doi.org/10.1038/nrn2667

Bandyopadhyay, S., Shamma, S. A., & Kanold, P. O. (2010). Dichotomy of functional organization in the mouse auditory cortex. *Nature Neuroscience*, *13*(3), 361-368. https://doi.org/10.1038/nn.2490

Brodmann, K. (1909). *Vergleichende Lokalisationslehre der Grosshirnrinde in ihren Prinzipien dargestellt auf Grund des Zellenbaues*. Barth.

Buschman, T. J., Siegel, M., Roy, J. E., & Miller, E. K. (2011). Neural substrates of cognitive capacity limitations. *Proceedings of the National Academy of Sciences*, *108*(27), 11252-11255. https://doi.org/10.1073/pnas.1104666108

Buzsáki, G., Anastassiou, C. A., & Koch, C. (2012). The origin of extracellular fields and currents-EEG, ECoG, LFP and spikes. *Nature Reviews Neuroscience*, *13*(6), 407-420. https://doi.org/10.1038/nrn3241

Canolty, R. T., & Knight, R. T. (2010). The functional role of cross-frequency coupling. *Trends in Cognitive Sciences*, *14*(11), 506-515. https://doi.org/10.1016/J.TICS.2010.09.001

Chapeton, J. I., Wittig, J. H., Inati, S. K., & Zaghloul, K. A. (2022). Micro-scale functional modules in the human temporal lobe. *Nature Communications*, *13*(1). https://doi.org/10.1038/s41467-022-34018-w

Chen, Y., Bressler, S. L., & Ding, M. (2006). Frequency decomposition of conditional Granger causality and application to multivariate neural field potential data. *Journal of neuroscience methods*, *150*(2), 228-237. https://doi.org/10.1016/J.JNEUMETH.2005.06.011

Eisenkolb, V. M., Held, L. M., Utzschmid, A., Lin, X.-X., Krieg, S. M., Meyer, B., Gempt, J., & Jacob, S. N. (2023). Human acute microelectrode array recordings with broad cortical access, single-unit resolution, and parallel behavioral monitoring. *Cell Reports*, *42*(5). https://doi.org/10.1016/j.celrep.2023.112467

Epstein, R., & Kanwisher, N. (1998). A cortical representation of the local visual environment. *Nature*, *392*(6676), 598-601. https://doi.org/10.1038/33402

Fedorenko, E., Behr, M. K., & Kanwisher, N. (2011). Functional specificity for high-level linguistic processing in the human brain. *Proceedings of the National Academy of Sciences*, *108*(39), 16428-16433. https://doi.org/10.1073/pnas.1112937108

Fedorenko, E., Duncan, J., & Kanwisher, N. (2013). Broad domain generality in focal regions of frontal and parietal cortex. *Proceedings of the National Academy of Sciences*, *110*(41), 16616-16621. https://doi.org/10.1073/pnas.1315235110

Fodor, J. A. (1983). *The modularity of mind*. MIT press. https://doi.org/10.7551/mitpress/4737.001.0001

Gordon, E. M., Chauvin, R. J., Van, A. N., Rajesh, A., Nielsen, A., Newbold, D. J., Lynch, C. J., Seider, N. A., Krimmel, S. R., & Scheidter, K. M. (2023). A somato-cognitive action network alternates with effector regions in motor cortex. *Nature*, *617*(7960), 351-359. https://doi.org/10.1038/s41586-023-05964-2

Granger, C. W. (1969). Investigating causal relations by econometric models and cross-spectral methods. *Econometrica: journal of the Econometric Society*, 424-438. https://doi.org/10.2307/1912791

Hanganu-Opatz, I. L., Klausberger, T., Sigurdsson, T., Nieder, A., Jacob, S. N., Bartos, M., Sauer, J.-F., Durstewitz, D., Leibold, C., & Diester, I. (2023). Resolving the prefrontal mechanisms of adaptive cognitive behaviors: A cross-species perspective. *Neuron*, *111*(7), 1020-1036. https://doi.org/10.1016/j.neuron.2023.03.017

Harvey, B. M., Klein, B. P., Petridou, N., & Dumoulin, S. O. (2013). Topographic Representation of Numerosity in the Human Parietal Cortex. *Science*, *341*(6150), 1123-1126. https://doi.org/10.1126/science.1239052

Hubel, D. H., & Wiesel, T. N. (1977). Ferrier lecture-Functional architecture of macaque monkey visual cortex. *Proceedings of the Royal Society of London. Series B. Biological Sciences*, *198*(1130), 1-59. https://doi.org/10.1098/rspb.1977.0085
Humphries, C., Liebenthal, E., & Binder, J. R. (2010). Tonotopic organization of human auditory cortex. *NeuroImage*, *50*(3), 1202-1211. https://doi.org/10.1016/j.neuroimage.2010.01.046
Jacob, S. N., Hähnke, D., & Nieder, A. (2018). Structuring of Abstract Working Memory Content by Fronto-parietal Synchrony in Primate Cortex. *Neuron*, *99*(3), 588-597.e585. https://doi.org/10.1016/j.neuron.2018.07.025
Jacob, S. N., & Nieder, A. (2014). Complementary roles for primate frontal and parietal cortex in guarding working memory from distractor stimuli. *Neuron*, *83*(1), 226-237. https://doi.org/10.1016/j.neuron.2014.05.009
Jacob, S. N., Stalter, M., & Nieder, A. (2016). Cell-type-specific modulation of targets and distractors by dopamine D1 receptors in primate prefrontal cortex. *Nature Communications*, *7*(1), 1-11. https://doi.org/10.1038/ncomms13218
Jung, J., Lambon Ralph, M. A., & Jackson, R. L. (2022). Subregions of DLPFC Display Graded yet Distinct Structural and Functional Connectivity. *The Journal of Neuroscience*, *42*(15), 3241-3252. https://doi.org/10.1523/jneurosci.1216-21.2022
Kaas, J. H. (1997). Topographic maps are fundamental to sensory processing. *Brain research bulletin*, *44*(2), 107-112. https://doi.org/10.1016/S0361-9230(97)00094-4
Kanwisher, N. (2010). Functional specificity in the human brain: A window into the functional architecture of the mind. *Proceedings of the National Academy of Sciences*, *107*(25), 11163-11170. https://doi.org/10.1073/pnas.1005062107
Kanwisher, N., Mcdermott, J., & Chun, M. M. (1997). The Fusiform Face Area: A Module in Human Extrastriate Cortex Specialized for Face Perception. *The Journal of Neuroscience*, *17*(11), 4302-4311. https://doi.org/10.1523/jneurosci.17-11-04302.1997
Karvat, G., Alyahyay, M., & Diester, I. (2021). Spontaneous activity competes with externally evoked responses in sensory cortex. *Proceedings of the National Academy of Sciences of the United States of America*, *118*(25). https://doi.org/10.1073/pnas.2023286118
Katzner, S., Nauhaus, I., Benucci, A., Bonin, V., Ringach, D. L., & Carandini, M. (2009). Local Origin of Field Potentials in Visual Cortex. *Neuron*, *61*(1), 35-41. https://doi.org/10.1016/j.neuron.2008.11.016
Koechlin, E., Ody, C., & Kouneiher, F. (2003). The architecture of cognitive control in the human prefrontal cortex. *Science*, *302*(5648), 1181-1185. https://doi.org/10.1126/science.1088545
Lashley, K. S. (1950). In search of the engram.
Liebe, S., Hoerzer, G. M., Logothetis, N. K., & Rainer, G. (2012). Theta coupling between V4 and prefrontal cortex predicts visual short-term memory performance. *Nature Neuroscience*, *15*(3), 456-462. https://doi.org/10.1038/nn.3038
Lin, X.-X., Nieder, A., & Jacob, S. N. (2023). The neuronal implementation of representational geometry in primate prefrontal cortex. *Science Advances*, *9*(50). https://doi.org/10.1126/sciadv.adh8685
Lindén, H., Tetzlaff, T., Potjans, T. C., Pettersen, K. H., Grün, S., Diesmann, M., & Einevoll, G. T. (2011). Modeling the spatial reach of the LFP. *Neuron*, *72*(5), 859-872. https://doi.org/10.1016/j.neuron.2011.11.006
Lundqvist, M., Brincat, S. L., Rose, J., Warden, M. R., Buschman, T. J., Miller, E. K., & Herman, P. (2023). Working memory control dynamics follow principles of spatial computing. *Nature Communications*, *14*(1), 1429. https://doi.org/10.1038/s41467-023-36555-4
Lundqvist, M., Herman, P., Warden, M. R., Brincat, S. L., & Miller, E. K. (2018). Gamma and beta bursts during working memory readout suggest roles in its volitional control. *Nature Communications*, *9*(1). https://doi.org/10.1038/s41467-017-02791-8
Lundqvist, M., Rose, J., Herman, P., Brincat, Scott L. L., Buschman, Timothy J. J., & Miller, Earl K. K. (2016). Gamma and Beta Bursts Underlie Working Memory. *Neuron*, *90*(1), 152-164. https://doi.org/10.1016/j.neuron.2016.02.028
Mansouri, F. A., Koechlin, E., Rosa, M. G. P., & Buckley, M. J. (2017). Managing competing goals — a key role for the frontopolar cortex. *Nature Reviews Neuroscience*, *18*(11), 645-657. https://doi.org/10.1038/nrn.2017.111

Mccandliss, B. D., Cohen, L., & Dehaene, S. (2003). The visual word form area: expertise for reading in the fusiform gyrus. *Trends in Cognitive Sciences*, *7*(7), 293-299. https://doi.org/10.1016/s1364-6613(03)00134-7

Miller, E. K., Lundqvist, M., & Bastos, A. M. (2018). Working Memory 2.0. *Neuron*, *100*(2), 463-475. https://doi.org/10.1016/J.NEURON.2018.09.023

Moca, V. V., Bârzan, H., Nagy-Dăbâcan, A., & Mureșan, R. C. (2021). Time-frequency super-resolution with superlets. *Nature Communications 2021 12:1*, *12*(1), 1-18. https://doi.org/10.1038/s41467-020-20539-9

Mongillo, G., Barak, O., & Tsodyks, M. (2008). Synaptic Theory of Working Memory. *Science*, *319*(5869), 1543-1546. https://doi.org/10.1126/SCIENCE.1150769

Nieder, A., Freedman, D. J., & Miller, E. K. (2002). Representation of the quantity of visual items in the primate prefrontal cortex. *Science*, *297*(5587), 1708-1711. https://doi.org/10.1126/science.1072493

Ostojic, S., & Fusi, S. (2024). Computational role of structure in neural activity and connectivity. *Trends in Cognitive Sciences*, *28*(7), 677-690. https://doi.org/10.1016/j.tics.2024.03.003

Penfield, W., & Boldrey, E. (1937). Somatic motor and sensory representation in the cerebral cortex of man as studied by electrical stimulation. *Brain*, *60*(4), 389-443. https://doi.org/10.1093/brain/60.4.389

Pesaran, B., Nelson, M. J., & Andersen, R. A. (2008). Free choice activates a decision circuit between frontal and parietal cortex. *Nature*, *453*(7193), 406-409. https://doi.org/10.1038/nature06849

Petrides, M., & Pandya, D. N. (1984). Projections to the frontal cortex from the posterior parietal region in the rhesus monkey. *Journal of Comparative Neurology*, *228*(1), 105-116. https://doi.org/10.1002/cne.902280110

Petrides, M., & Pandya, D. N. (1999). Dorsolateral prefrontal cortex: comparative cytoarchitectonic analysis in the human and the macaque brain and corticocortical connection patterns. *European Journal of Neuroscience*, *11*(3), 1011-1036. https://doi.org/10.1046/j.1460-9568.1999.00518.x

Rapan, L., Froudist-Walsh, S., Niu, M., Xu, T., Zhao, L., Funck, T., Wang, X.-J., Amunts, K., & Palomero-Gallagher, N. (2023). Cytoarchitectonic, receptor distribution and functional connectivity analyses of the macaque frontal lobe. *eLife*, *12*, e82850. https://doi.org/10.7554/eLife.82850

Rigotti, M., Barak, O., Warden, M. R., Wang, X.-J., Daw, N. D., Miller, E. K., & Fusi, S. (2013). The importance of mixed selectivity in complex cognitive tasks. *Nature*, *497*(7451), 585-590. https://doi.org/10.1038/nature12160

Riley, M. R., Qi, X.-L., Zhou, X., & Constantinidis, C. (2018). Anterior-posterior gradient of plasticity in primate prefrontal cortex. *Nature Communications*, *9*(1). https://doi.org/10.1038/s41467-018-06226-w

Salazar, R. F., Dotson, N. M., Bressler, S. L., & Gray, C. M. (2012). Content-Specific Fronto-Parietal Synchronization During Visual Working Memory. *Science*, *338*(6110), 1097-1100. https://doi.org/10.1126/science.1224000

Schreiner, C. E., Read, H. L., & Sutter, M. L. (2000). Modular organization of frequency integration in primary auditory cortex. *Annual Review of Neuroscience*, *23*(1), 501-529. https://doi.org/10.1146/annurev.neuro.23.1.501

Seedat, Z. A., Quinn, A. J., Vidaurre, D., Liuzzi, L., Gascoyne, L. E., Hunt, B. A., O'neill, G. C., Pakenham, D. O., Mullinger, K. J., & Morris, P. G. (2020). The role of transient spectral 'bursts' in functional connectivity: A magnetoencephalography study. *NeuroImage*, *209*, 116537. https://doi.org/10.1016/j.neuroimage.2020.116537

Siegel, M., Warden, M. R., & Miller, E. K. (2009). Phase-dependent neuronal coding of objects in short-term memory. *Proceedings of the National Academy of Sciences of the United States of America*, *106*(50), 21341-21346. https://doi.org/10.1073/pnas.0908193106

Steel, A., Silson, E. H., Garcia, B. D., & Robertson, C. E. (2024). A retinotopic code structures the interaction between perception and memory systems. *Nature Neuroscience*, *27*(2), 339-347. https://doi.org/10.1038/s41593-023-01512-3

Stokes, M. G. (2015). 'Activity-silent' working memory in prefrontal cortex: A dynamic coding framework. *Trends in Cognitive Sciences*, *19*(7), 394-405. https://doi.org/10.1016/j.tics.2015.05.004

Talbot, S., & Marshall, W. (1941). Physiological studies on neural mechanisms of visual localization and discrimination. *American Journal of Ophthalmology*, *24*(11), 1255-1264. https://doi.org/10.1016/S0002-9394(41)91363-6

Tye, K. M., Miller, E. K., Taschbach, F. H., Benna, M. K., Rigotti, M., & Fusi, S. (2024). Mixed selectivity: Cellular computations for complexity. *Neuron*. https://doi.org/10.1016/j.neuron.2024.04.017

Vinck, M., van Wingerden, M., Womelsdorf, T., Fries, P., & Pennartz, C. M. (2010). The pairwise phase consistency: a bias-free measure of rhythmic neuronal synchronization. *NeuroImage*, *51*(1), 112-122. https://www.sciencedirect.com/science/article/pii/S1053811910000959?via%3Dihub

Wang, S., Falcone, R., Richmond, B., & Averbeck, B. B. (2023). Attractor dynamics reflect decision confidence in macaque prefrontal cortex. *Nature Neuroscience*, *26*(11), 1970-1980. https://doi.org/10.1038/s41593-023-01445-x

Wang, X. J. (2010). Neurophysiological and computational principles of cortical rhythms in cognition. *Physiological reviews*, *90*(3), 1195-1268. https://doi.org/10.1152/physrev.00035.2008

Xie, Y., Hu, P., Li, J., Chen, J., Song, W., Wang, X.-J., Yang, T., Dehaene, S., Tang, S., Min, B., & Wang, L. (2022). Geometry of sequence working memory in macaque prefrontal cortex. *Science*, *375*(6581), 632-639. https://doi.org/10.1126/science.abm0204